

The Relevance of Measurement Systems Analysis

A Procter & Gamble Case Study on
MSA Methodology and Applications

DATE

**OCTOBER
10 AND 12**

TIME

**16:00 CET,
10 am EST**



**CHRISTIAN
NEU**

Scientist
Procter & Gamble



**JERRY
FISH**

Systems Engineer
JMP



**JASON
WIGGINS**

Senior Systems
Engineer
JMP

Register now

Rubber-Like Soft Lattice Structure for Anti-Ballooning in Fluidic Elastic Soft Robots

Liang He,* Sihan Wang, and Perla Maiolino

Additive manufacturing of lattice structures provides materials with enhanced strength, stiffness, and lightweight properties. While most research focuses on stiff, low-stretch materials like metals and acrylonitrile butadiene styrene, herein, the tensile behavior of soft, elastomeric lattice structures is explored. Soft-material 3D-printing advancements have enabled increased usage of directly printed soft robots. Traditional fluidic elastic actuators, however, face limitations due to the ballooning effect of soft polymers, causing potential explosions or leakages. To mitigate this, the study proposes using a soft lattice structure to reinforce soft inflatable robots, thereby reducing the ballooning effect and increasing design freedom. Herein, soft lattices are fabricated using Agilus30 in a Stratasys J735 printer and their behaviors under compression and stretching are compared. It is indicated in the results that lattice reinforcement maintains the soft robot's shape under higher pressure and allows tunability of stiffness with variable internal pressure. The implementation of this method in non-convex soft robots successfully demonstrates its anti-ballooning effect.

development of soft materials for the fabrication and 2) the structure design and computational optimization of the robot.

Recent advances in soft-material 3D-printing technologies have shown promising results for the fabrication of soft actuators with optimized structure design.^[4,5] Although casting with silicone rubber has been the most commonly used method for the fabrication of soft robots for the past 3 decades, soft-material additive manufacturing is catching up with many incremental works within the last 10 years with increased performance in repeatability, design freedom, accuracy, and fabrication speed.^[6–8]

Among the broad family of soft actuators, fluidic elastic actuator (FEA) is particularly favored with soft-material 3D printing due to its high compliance and simplicity in control.^[9] The actuation of


1. Introduction

Recent soft-robotic applications in minimally invasive surgery,^[1] human–robot interaction,^[2] and delicate object manipulation^[3] demonstrate the advantages of introducing soft and compliant mechanisms in many industrial scenarios. The soft interface actuated with simplified control strategies allows a safe and adaptive interaction between the object and the robot. This reduces manufacturing and computational cost, which usually requires expensive sensors and precise mechanical actuators for feedback control. The key to soft-robotic research is to investigate how the actuation of the robot can work collaboratively with the inherited compliance of the material to provide stiffness and morphology changing to generate desired motion and interaction with the environment. Thus, the development relies on 1) the

FEAs relies on inflation via internal pressurization. A critical limitation of such a method is the ballooning effect of the soft polymers, commonly defined as the unnecessary inflation of the robot in an undesired area. In the design of FEA, undesired ballooning could result in a waste of energy, less effective motion, and excessive stretching of the material that increases the risk of break/failure. This usually has been addressed by attaching external sheathing, or fiber reinforcement in the FEA.^[10] In the development of tunable stiffness mechanisms based on internal pressure, the undesired ballooning effect could also cause a side effect on the object geometry change. For instance, in the design of a soft-pneumatic-based tactile sensor proposed in ref. [11], the internal pressure was used as a mechanism to change the stiffness of the sensor, where a geometry change of the sensor is observed due to the ballooning effect.

In general, anti-ballooning in soft robotics can usually be achieved by two methods 1) introducing composite material and 2) designing functionally graded structural elements to create anisotropic stiffness distribution to articulate actuation motion with distributed pressure via pneumatic or hydraulic solutions. Both methods require a complicated manufacturing process with conventional casting (investment casting or layered casting), thus, limiting their applications. Additive manufacturing, in contrast, provided the potential to fabricate functionally graded structural elements that can significantly increase the design freedom of the FEA actuators. The soft-robotic hand developed by Shorthose et al. utilized multi-material 3D printing to limit unnecessary ballooning.^[12] Yet, composite material 3D printing still requires high fabrication costs. Bellow geometry

L. He, S. Wang, P. Maiolino
Department of Engineering Science
University of Oxford
Oxford ox2 6NN, UK
E-mail: Liang.he@eng.ox.ac.uk

 The ORCID identification number(s) for the author(s) of this article can be found under <https://doi.org/10.1002/adem.202300534>.

© 2023 The Authors. Advanced Engineering Materials published by Wiley-VCH GmbH. This is an open access article under the terms of the Creative Commons Attribution License, which permits use, distribution and reproduction in any medium, provided the original work is properly cited.

DOI: 10.1002/adem.202300534

as a design feature to create anisotropic stiffness distribution of single-material soft robots is widely seen in recent research.^[13]

In addition to these widely used anti-ballooning methods to 3D print soft robots, designing FEAs with soft lattice reinforcement (an almost impossible structure to be fabricated with conventional casting solutions) shows a new solution in fabrication.^[14,15]

Cellular solids with repeated cell structures have been an important engineering application for additive manufacturing due to the high stiffness-to-density ratio and their ability to fabricate functionally graded material (FGM) with controllable stiffness, density, and anisotropy.^[16,17] The application of rigid lattice structure has been intensively studied to produce aerospace parts or medical implants via fabricating metal components with selective laser melting,^[18] electron beam melting,^[19] and powder bed fusion.^[20,21] Polymer-based lattice (non-stretchable) has also been studied with stereolithography,^[22] selective laser sintering,^[23] and material extrusion.^[24] However, the applications of soft and stretchable lattice structures are still in their infancy.^[25,26]

The fast development of soft-material 3D printing and its application in monolithically fabrication soft robots urges this study to introduce and characterize soft lattice structure as FGM for fluidic elastic soft-robot design.

In this article, we proposed to deploy 3D-printed soft lattice structures in the design of fluidic elastic soft robots for anti-ballooning, investigating the role of lattice type, unit size, and strut thickness. Soft lattices with four different lattice types (“X”, “Grid”, “Vintiles”, and “Cross”) and various unit sizes were fabricated with Agilus30 in a Stratasys J735 printer, with the mechanical characterization done in both compression and tensile tests. A finite-element analysis was also conducted to evaluate the mechanical response of the soft lattice. A demonstration of applying the soft lattice in tunable stiffness tumor simulation is shown.

The rest of the paper is structured as follows. The section Experimental Section provides the details of the soft lattice design and experiment setups. The design of the soft and stretchable lattice is introduced in Section 2.1. The material of the soft lattice is described in Section 2.2. Finite-element (FE) simulation was used to study the mechanical behavior of the different soft lattice design, the specification and setup are included in Section 2.3. The methodology and setup for the compression and tensile test, fatigue test, anti-ballooning, and increase of stiffness experiment were described in Section 2.4–2.7, respectively. The results of the tests are further provided and discussed in Section 3. A demonstration of applying the soft lattice in tunable stiffness tumor simulation is included in Section 3.7.

2. Materials and Methodology

2.1. Design of the Soft and Stretchable Lattice

In this study, each lattice unit was designed as a cellular cube with a unit length of a . The individual lattice cell was modeled by the spacial arrangement of connection nodes with the diameter of D_0 and cylindrical struts with the diameter of d for reinforcement. The schematics of the lattice unit are illustrated in **Figure 1**. Four types of soft lattice cells were designed and studied: “X”, “Grid”, “Vintiles”, and “Cross” (**Figure 1c**). Lattice-type “X” consisted of 8 connection nodes at the vertices of the cellular

cube with struts between each pair of body diagonals. Lattice-type “Grid” consisted of 8 connection nodes at the vertices of the cellular cube with struts to form the edges of the cube. Lattice-type “Vintiles” consisted of 28 connection nodes with struts to form a hexagon cube. Lattice-type “Cross” consisted of 8 connection nodes at the vertices of the cellular cube with struts between each pair of surface diagonals. Lattice-reinforced soft robots were created when the cellular unit cube was populated in a soft inflatable actuator to create an internal lattice topology. An example of lattice reinforced non-convex pneumatic soft robot is shown in **Figure 1b**, a simulated tumor used for medical examination training. Applying positive pressure to the simulated tumor increased the stiffness, while the soft lattice reinforcement would provide constraint to maintain the non-convex surface geometry and texture.

2.2. Materials

All soft lattice units were designed with CAD software (Solidworks 2020) and fabricated with Agilus30 (Stratasys Ltd, USA), a soft and rubber-like material with a quoted tensile strength of 2.4–3.1 MPa, an elongation at break of 220%–270% and a shore hardness of 30 A. Agilus30 was chosen in this study due to its softness and its wide use in the soft-robotics community to develop FEAs.^[11,27,28] However, the application of developing FEA with lattice reinforcement was not investigated.

2.3. FE Method Simulation

FE method (FEM) was used to study the mechanical response of the soft lattice structure in compression and tensile conditions.^[29] The soft lattice samples were modeled with $2 \times 2 \times 3$ units of lattice elements (each unit dimension is $5 \times 5 \times 5$ mm), aiming to investigate the effect of soft lattice types. The compression testing condition represented a soft robot with lattice reinforcement under external loading. The structural design of the lattice elements would increase the baseline stiffness of the soft robot due to the reinforcement. The tensile testing condition represented a soft robot with lattice reinforcement during inflation with increased internal driving pressure. The structural design of the lattice elements would introduce constraints to the soft-robot inflation, therefore, reducing the undesired ballooning effect.

2.4. Compression and Tensile Test

Experimental characterization was conducted with the 3D-printed soft lattice samples to study the mechanical response. The compression and tensile test were performed with a 3-axis cartesian robot. An indenter with a load cell is attached to the cartesian robot to measure the loading conditions. The schematics of the experiment setup in indicated in **Figure 2a**.

In the compression test, the soft lattice response was characterized by bringing the indenter into contact with the sample up to 6 mm displacement with the step size of 0.5 mm increment and the speed of 5 mm s^{-1} . At each step, the indenter was waited 5 s to ensure enough relaxation of the material. The maximum indentation 6 mm is equivalent to 40% of the height of the soft

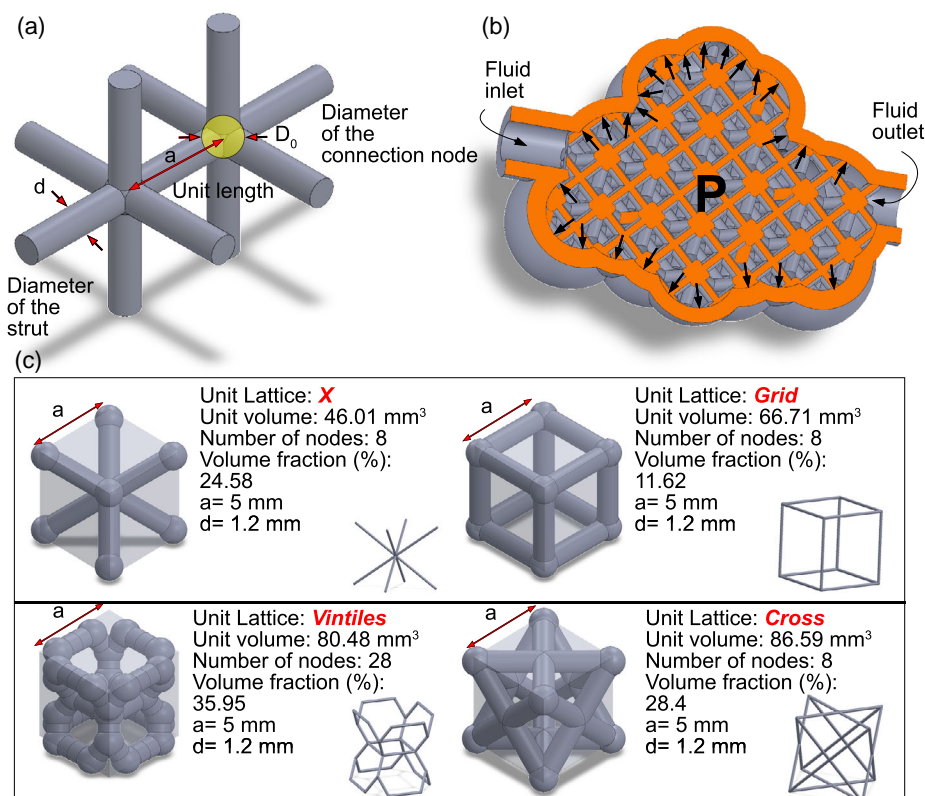


Figure 1. a) A schematic of the lattice reinforcement. The thickness of the strut is defined with the diameter of the cylinder d . The unit length a is used to define the size of a lattice element. A spherical node with the diameter of D_0 is used for the strut connection. b) A demonstration of lattice reinforcement for anti-ballooning of a pressurized non-convex soft structure. The lattice structure ensured the flow of the driving fluid while maintaining the constraint for the enclosed soft structure. c) The design of the four types of lattice units studied in this paper: “X”, “Grid”, “Vintiles”, and “Cross.” The parameters lattice type, unit volume, number of nodes, volume fraction (%), unit length a , and diameter of the strut d were used to characterize the specifications of the design.

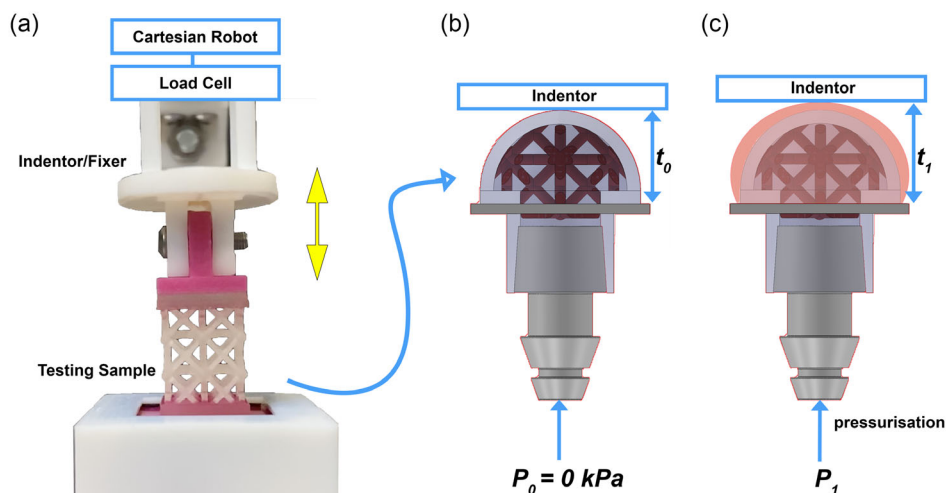


Figure 2. Experimental setup for the characterization of the mechanical response of the soft lattice structure. a) The 3D-printed lattice testing sample is mounted with a cartesian robot and a load cell. Samples with an internal cavity for pressurization are placed in the setup while connecting a pressure control system. b) The sample at its original state with internal pressure $P_0 = 0$ kPa. c) The sample at a pressurized state with internal pressure P_1 to show the anti-ballooning effect of the lattice reinforcement.

lattice sample. Once the 6 mm maximum indentation is reached, the load is removed with the same step size decrement. This procedure was repeated 3 times for each sample. Four types of soft lattices “X”, “Grid”, “Vintiles”, and “Cross” were studied. All samples were designed with strut diameter $d = 1.0$ mm.

In the tensile test, the soft lattice response was characterized by bringing the fixer away from the sample up to failure (the sample torn up) with the step size of 0.2 mm increment and the speed of 5 mm s^{-1} . At each step, the indenter was also waited 5 s to ensure enough relaxation of the material. Two sets of tensile tests were performed to study the effect of lattice type and strut thickness, respectively. To study the effect of lattice type, four types of soft lattices “X”, “Grid”, “Vintiles”, and “Cross” were studied. All samples were designed with strut diameter $d = 1.0$ mm. To study the effect of strut thickness, samples with strut diameter $d = 0.8, 1.0, 1.2, 1.4$, and 1.6 mm were tested. All samples were designed with soft lattice “Cross.” Three identical testing pieces were characterized for each sample type.

2.5. Fatigue Test

To act as an effective anti-ballooning solution for pneumatic-driven soft robots, the soft lattice structure needs to ensure high durability to withhold repeated pressurization and compression during actuation. This experiment analyzed the effect of strut thickness with repeated fatigue tests. The fatigue tests are performed by repeatedly indenting the sample up to 4 mm and pulling the sample up to 2 mm for 500 working cycles. Five samples with strut diameter $d = 1.6, 1.4, 1.2, 1.0$, and 0.8 mm were tested. All soft lattice samples were designed with “Cross” reinforcement. The force during the test is recorded with the load cell.

2.6. Anti-Ballooning Experiment with Inflatable Soft Lattice

The effect of anti-ballooning was evaluated by designing a 3D-printed hemispherical shell with soft lattice reinforcement, shown in Figure 2b. The samples were connected to a pressure regulator to adjust the internal pressure and placed underneath the load cell and the cartesian robot to measure the sample size (t) during pressurization, representing the ballooning condition (Figure 2c). Sample size (t) is measured by bringing down the indenter to detect the contact surface to record the increase in its height. The samples were pressurized until their height reached 125% of the original diameter with a step increment of 5 kPa. The experiment was repeated three times for each sample.

One sample with no lattice reinforcement and three samples with lattice unit sizes of 4, 5, and 6 mm were tested. All lattice reinforcement was designed with a “Cross”-type lattice with the strut diameter $d = 1.0$ mm. The force during the test was recorded with the load cell.

2.7. Increase of Stiffness with Inflatable Soft Lattice

The effect of soft lattice reinforcement for allowing the soft robot to be driven at a higher pressure with increased stiffness was studied in this experiment. The characterization was done with the same setup shown in Figure 2 and described in Section 2.6. The same testing samples were used as the samples described in

Section 2.6. After pre-pressurizing the sample to a certain pressure level, an indentation test was performed on the sample. The displacement of the indenter and the response force was measured to represent the stiffness of the sample with increased driving pressure. A spherical sample of the same geometry as the non-pressurized sample made of silicone (Ecoflex0030, Smooth-on) was also characterized with the same methodology as a benchmark of stiffness.

3. Result and Discussion

3.1. FEM

The FEM result of the tensile test shows that the level of constraint the lattice structure can provide when being used as an anti-ballooning solution for pneumatic-driven soft robots. The simulation is shown in Figure 3. The equivalent elastic strain is shown. The result of the simulation is presented in Figure 4. The elongation ϵ is computed by $\epsilon = (D + D_0)/D_0$, where D is the displacement of the top plate of the sample, D_0 is the original height of the sample 13 mm. When the lattice structures have the same strut diameter and unit size, lattice-type “Vintiles” provided the greatest constraint for anti-ballooning, followed by lattice-type “Cross” and “Grid.” Lattice-type “X” provided considerably lower constraint compared to other types.

A linear model was employed to characterize the response of the sample, primarily due to its simplicity and the ease of comparison across different lattice samples. We can define a constraint ratio, C , as the slope of this linear model. Subsequently, a constraint coefficient can be computed, taking into consideration both the constraint ratio and the quantity of material used. By fitting a linear model to the data $\Delta\sigma/\Delta\epsilon$, a constraint ratio C can be determined as 5.8792, 4.0891, 2.9868, and 1.2622 for lattice-type “Vintiles”, “Cross”, “Grid”, and “X”, respectively.

The coefficient of constraint K is computed by defining $K = C/V$, where C is the constraint ratio and V is the volume fraction of the soft lattice in the unit-length cellular cube, representing the amount of material used. The result of the coefficient of constraint K of different lattice types is shown in Figure 5.

Similarly, the study of compression simulation is demonstrated in Figure 3. The result is shown in Figure 6. The lattice-type “Vintiles” shows the highest stiffness, followed by “cross” and “grid”. The “X”-type lattice reinforcement shows the lowest stiffness in the compression simulation. This is in alignment with the simulation result of the tensile test. It needs to be noted that the simulation is only carried up to the maximum displacement that caused the failure of the model. The lattice-type “Grid” exhibits the failure of the modeling with only 0.4 mm displacement, presumably, due to the structure buckling during compression. The effect of buckling will be discussed further, with the experimental result in the following section.

3.2. Experimental Result: The Effect of Lattice type

3.2.1. Buckling in Compression

The effect of soft lattice type in compression is shown in Figure 7. Although the unit size and strut thickness are the same

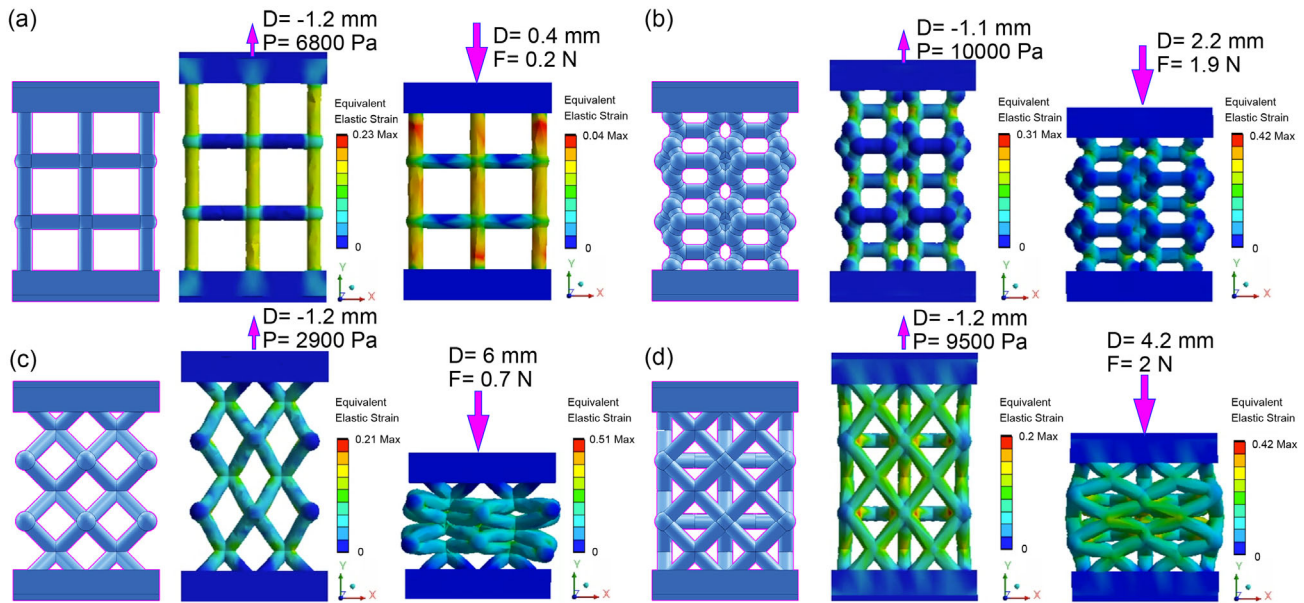


Figure 3. The finite-element method (FEM) simulation of the elongation and tensile test of the soft lattice structure with type a) “Grid”, b) “Vintiles”, c) “X”, and d) “Cross.” The original sample, its maximum displacement, and the simulated response of pressure and force are shown in the figure.

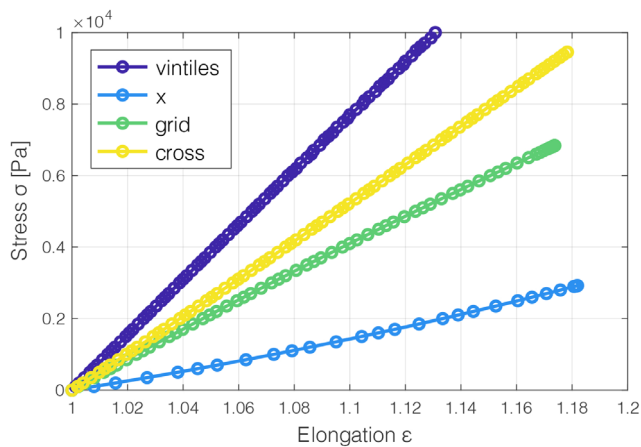


Figure 4. FEM simulation result of the tensile test on soft lattice types “Vintiles”, “Cross”, “Grid”, and “X.” The elongation ϵ is computed by $\epsilon = (D + D_0)/D_0$, where D is the displacement of the top plate of the sample, D_0 is the original height of the sample 13 mm.

for all samples, the lattice type with different reinforcement arrangements resulted in different mechanical responses in compression. A prominent bulking effect is exhibited with lattice-type “Grid” and “Vintiles” during the compression. For the “Grid”-type lattice, the bulking happens at an early phase with small deformation in compression. The increase of stiffness is also small with the “Grid”-type lattice reinforcement. For the “Vintiles”-type lattice, the buckling of individual units results in the shear distortion of the overall structure, with a gradually increased stress during the compression. This shear distortion also brings “Vintiles” the most significant amount of energy absorption, indicated by its largest hysteresis loop area shown

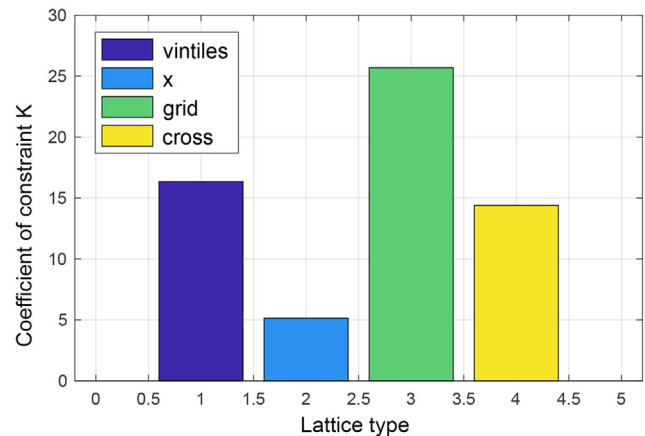


Figure 5. Computed coefficient of constraint K ($K = C/V$, where C is the constraint ratio and V is the volume fraction of the soft lattice in the unit-length cellular cube, representing the amount of material used.) for different lattice types based on the simulation result. This shows the amount of constraint the lattice structure can provide, considering the amount of material used.

in Figure 7. No noticeable buckling effect was observed for the lattice-type “X” and “Cross.” Sample with “X”-type lattice reinforcement shows an exponential increase of stiffness during the compression.

3.2.2. The Experiment of Tensile and Tearing Up

Figure 8 shows the result of the experimental tensile test. Lattice-type “Cross” can withhold the largest stress upon tearing. Lattice-type “X” can withhold the largest elongation upon

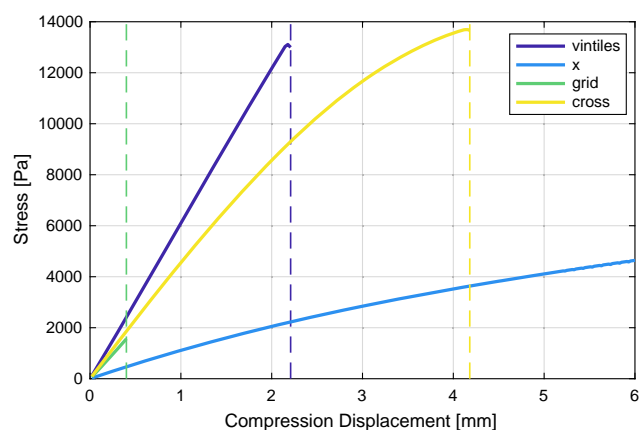


Figure 6. FEM simulation result of the compression test on soft lattice types “Vintiles”, “Cross”, “Grid”, and “X.” The simulation is only carried up to the maximum displacement that caused the failure of the model. The lattice-type “Grid” exhibits the failure of the modeling with only 0.4 mm displacement, presumably, due to the structure buckling.

tearing. It can also be observed that lattice types “Cross” and “Vintiles” tore up suddenly once the elongation reached their maximum. In contrast, lattice-type “Grid” and “X” tend to tear up gradually strand by strand upon the break of the entire lattice group.

3.3. The Effect of Strut Thickness

The result of the tensile test on samples with different strut thicknesses is shown in **Figure 9**. For samples with the same unit size and lattice type, a gradually increased maximum stress upon break is observed with the increase of strut diameter. However, the maximum elongation at break is kept similar regardless of the strut thickness. This implies that when using the lattice structure as anti-ballooning reinforcement of pneumatic-driven soft robots, the modification of strut thickness would not affect the maximum deformation the robot can withhold upon break.

3.4. Fatigue Loading Cycles

The strut thickness of the soft lattice structure plays an important role in the stiffness and constraint of the sample. The thickness of the strut also determines the fatigue of the structure under cyclic loading conditions. When designing and fabricating a soft robot with soft lattice reinforcement, fatigue is critical for the performance of the robot. With a continuous cyclic compression and tensile test performed on samples with different strut thicknesses up to 500 cycles each, **Figure 10** shows the result. The peak force at the maximum elongation and compression of the samples during the test were extracted and plotted in the figure. All samples with the lattice strut thickness greater or equal to 1.0 mm remain intact after the cyclic test without

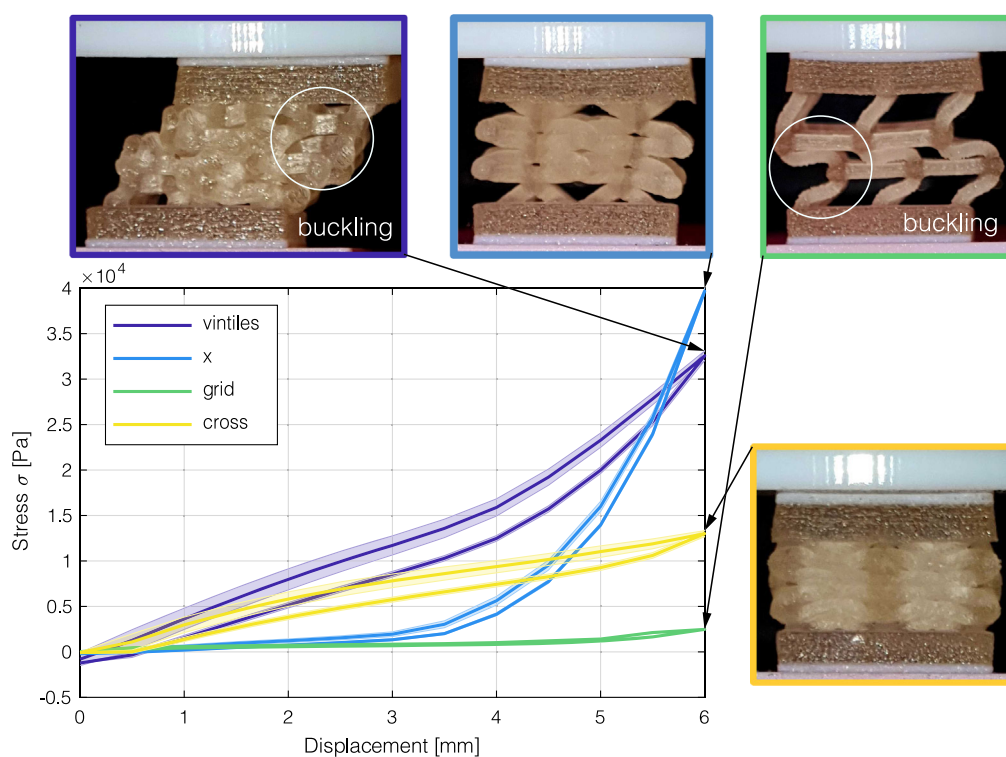


Figure 7. Experimental result of the compression test. A probe is used to press down the samples up to 6 mm displacement with a step size of 0.5 mm increment. Once the 6 mm maximum indentation is reached, the load is removed with the same step size. The standard deviation error of three trials of repeated tests is shown in the figure. Buckling of the soft lattice structure can be observed for the lattice-unit-type “vintiles” and “grid”, while the lattice-unit-type “cross” and “x” exhibits insignificant buckling during the 6 mm indentation. It can also be noted that lattice-unit-type “x” exhibits a nonlinear response of structure stiffness during the compression.

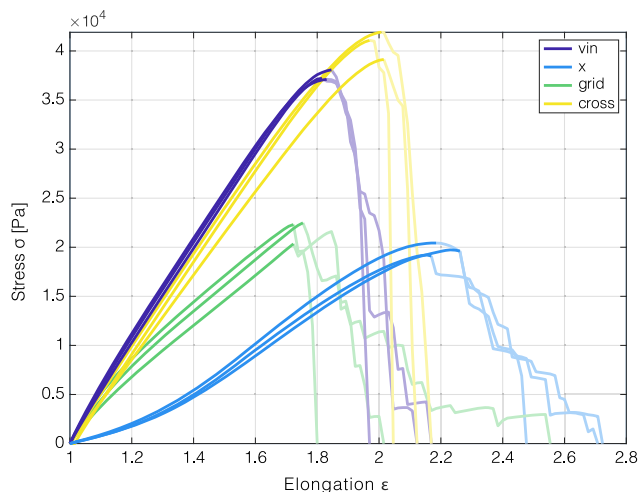


Figure 8. Experimental result of the tensile test on samples of four different lattice types. Three identical samples were tested for each type of the samples. The loading stress is continually collected after the sample reached its maximum elongation. A reduction in stress (marked with transparent lines) can be observed from the figure when the sample starts tearing up. The samples show a larger deviation of the mechanical response after the initial break of the sample, due to the small variations in manufacturing and loading conditions.

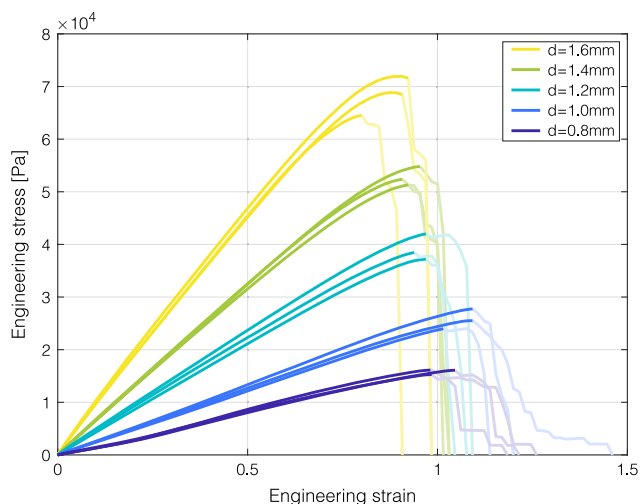


Figure 9. Experimental result of the tensile test on samples of different strut thicknesses. Three identical samples were tested for each type of sample. The loading stress is continually collected after the sample reaches its maximum elongation. A reduction of stress (marked with transparent lines) can be observed from the figure when the sample starts tearing up. An increase in stress can be observed for samples with increased strut diameter during the tensile test.

any tear-up of the lattice reinforcement. The lattice sample with strut diameter $d = 1.6$, 1.4 , and 1.2 mm shows minimum characteristics change of the material property, showing the stable and flat force response during the cyclic test. The lattice sample with strut diameter $d = 1.0$ mm also remained intact after the 500 cycles. However, a drop in the peak force response in the

elongation can be observed, indicating possible fatigue of the material. The lattice sample with strut diameter $d = 0.8$ mm failed the cyclic test at the 318th cycle with some lattice strand tearing up. However, part of the samples remained functional after the 500 cyclic tests.

3.5. The Effect of Lattice Unit Size and Its Performance in Anti-Ballooning

The result of the inflation ratio of the four half-spherical samples (no lattice, lattice unit size $d = 6$ mm, lattice unit size $d = 5$ mm, lattice unit size $d = 4$ mm) during pressurization is shown in **Figure 11**. A significant ballooning effect is exhibited for the sample without any lattice reinforcement with a 24.4% inflation ratio at 40 kPa during pressurization. The effect of anti-ballooning is demonstrated with all samples with lattice reinforcement. With a coarse reinforcement of lattice unit size $d = 6$ mm, the inflation ratio is reduced to 17.8% at 40 kPa. The finer reinforcement of lattice unit size $d = 5$ and 4 mm can further reduce the inflation ratio to around 14.2% at 40 kPa. The data shows a neglected reduction rate in the inflation ratio for lattice unit size $d = 5$ and 4 mm at the low-pressure range (less than 50 kPa). However, the effectiveness of anti-ballooning is shown with driving pressure higher than 50 kPa.

3.6. Increase Stiffness During Pressurization

The introduction of soft lattice reinforcement allows the inflatable soft robot to be driven at a higher pressure with increased stiffness. The result of the change of stiffness through an indentation test is shown in **Figure 12**. The compression rate indicates how much the sample was compressed in regard to its original height after pressurization. It needs to be noted that depending on the driving pressure and the sample type, the original height after pressurization of each experiment is different. In general, an increase in stiffness is shown with all samples with the increase of driving pressure. With the current design parameters, the soft structure shows a slightly higher stiffness than Ecoflex0030 in its non-pressurized state. Since all samples were pressurized until their height reached 125% of the original diameter, an increase in maximum driving pressure and stiffness is observed for samples with lattice reinforcement. The reduction of lattice size also increases its ability in increased stiffness with higher maximum driving pressure allowed.

3.7. Demonstration on Tunable Stiffness Tumor Simulations

To demonstrate the use of the proposed method, applying 3D-printed soft lattice structure in non-convex soft robots for anti-ballooning, the section shows the comparison of two 3D-printed tumor simulators with and without the soft lattice reinforcement. The 3D-printed tumors that can tune their stiffness with internal driving pressure is an effective way to simulate tumors in soft tissue for medical examination training.^[30,31] For instance, controlling the state of several tumors from soft to stiff (non-detectable and detectable) is effective in training manual palpation by embedding the tumors in simulated organs. In this study, two tumors with identical appearance are designed and 3D

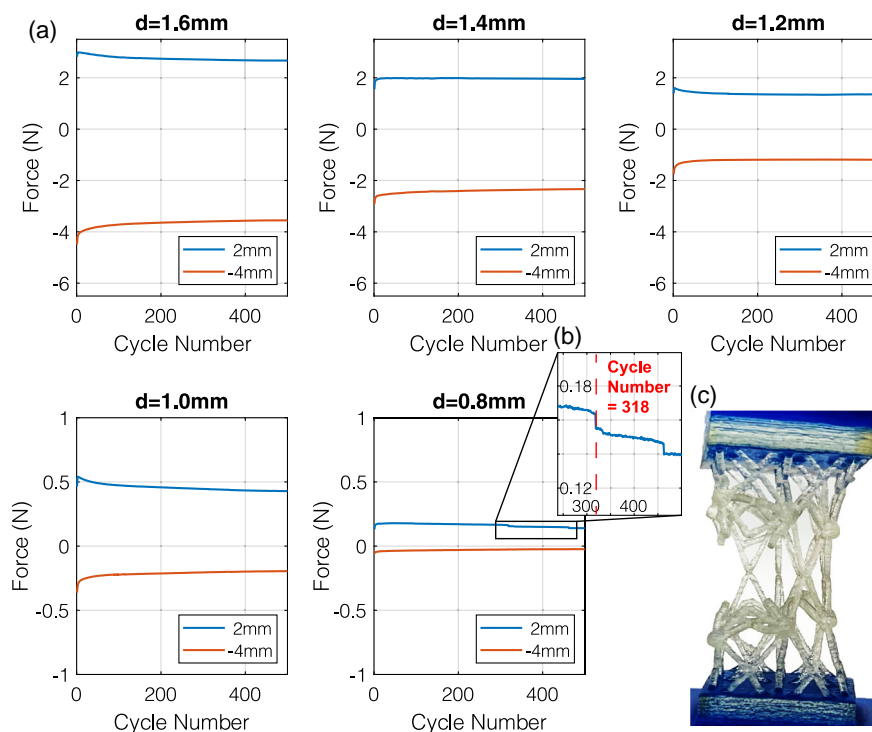


Figure 10. Experimental result of the fatigue test on samples of different strut thicknesses. a) The extracted peak force of the maximum elongation and compression of the sample during the 500 cycles of the test. b) An enlarged view of the data at cycle number = 318 where the soft lattice start tearing up. c) A picture of the lattice sample with strut thickness $d = 0.8$ mm after the 500 cycle fatigue test. Tearing up of several lattice strands can be observed.

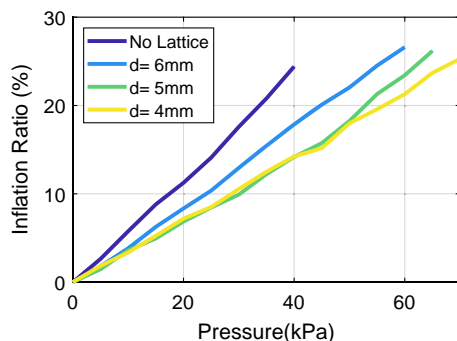


Figure 11. The result of the sample size change during inflation with gradually increased driving pressure. The effect of lattice unit size and its performance in anti-ballooning is demonstrated. The inflation ratio is computed as $(t_1/t_0) \times 100\%$, where t_1 is the measured sample height after pressurization and t_0 is the measured sample height before pressurization. The characterization data were collected with three times repetitions. The data shown in the figure represent the average at each driving pressure.

printed with Agilus30 using a Stratasys J735 printer (one with soft lattice reinforcement and one without any reinforcement). The “Cross”-type lattice with the strut diameter $d = 1.0$ mm and unit size of 5 mm is used for the anti-ballooning. The objective of the tumor simulation is to increase its stiffness with increased driving pressure while keeping the surface texture and fine features. **Figure 13** shows the experimental comparison

of the two types of tumors. It can be observed that the non-convex features of the tumor start disappearing after 16 kPa for the no-lattice reinforced sample. The sample shows almost a smooth surface texture with a driving pressure of 26 kPa. In contrast, the sample with lattice reinforcement maintained its non-convex features and kept the surface texture even at the driving pressure of 26 kPa.

4. Conclusion

This work investigated the utilization of soft lattice structures in 3D-printed soft pneumatic actuators to mitigate the ballooning effect, maintain non-convex features, and enhance its stiffness with higher driving pressure upon break. Both FEM and experimental studies evaluated different lattice types, unit sizes, and strut diameters. The results displayed significant buckling in “Grid” and “Vintiles” lattice types during compression, with “Grid” demonstrating minimal stiffness and “Vintiles” leading to shear distortions. However, the “X” and “Cross” lattices revealed no significant buckling. In terms of anti-ballooning reinforcement, “Vintiles” and “Cross” outperformed “Grid” and “X” at identical strut diameters and lattice sizes. Yet, in terms of material efficiency, the “Grid” lattice provided the highest coefficient of constraint. Experiments confirmed the effectiveness of soft lattices in reducing inflatable soft structure ballooning. By incorporating a lattice reinforcement with unit size $d = 4$ mm, the inflation ratio decreased from 24.4% to 14.2% at 40 kPa driving pressure.

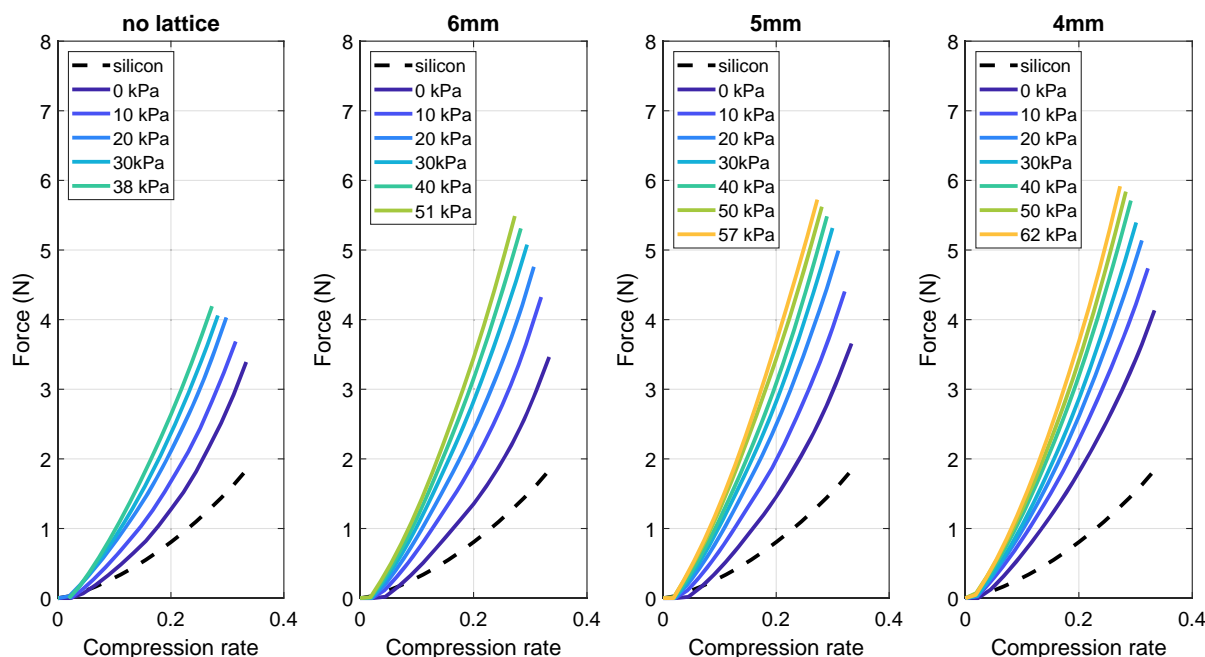


Figure 12. Experimental result of an inflation compression test. The data shows the result with samples with no lattice, with lattice unit sizes of 6, 5, and 4 mm. All lattice reinforcement is designed with a “Cross”-type lattice with the strut diameter $d = 1.0$ mm.

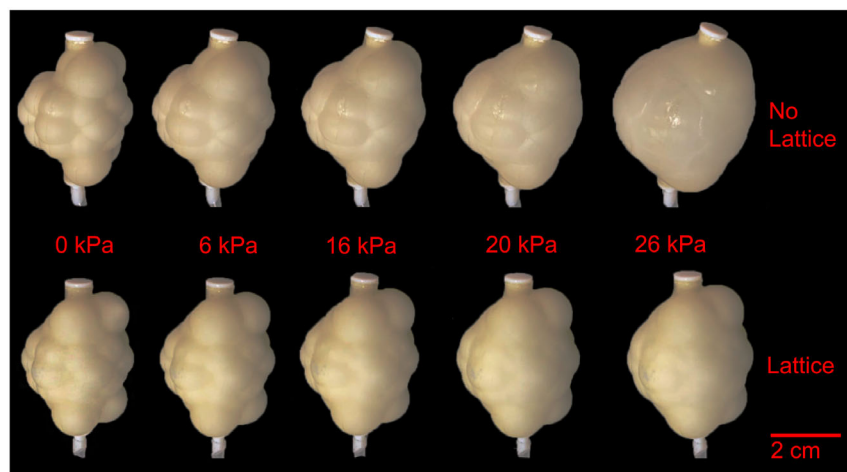


Figure 13. The 3D-printed tumor with increased driving pressure for increased stiffness. The comparison between samples with and without soft lattice reinforcement is shown in the bottom and top roll of the figure. The fine features and textures gradually disappeared with increased inflation on the 3D-printed tumors without soft lattice reinforcement. In contrast, the fine features were kept in much better detail for 3D-printed tumors with soft lattice reinforcement.

This study underscores the potential of 3D-printed soft lattice structures in enhancing stiffness and reducing ballooning in non-convex soft robots, expanding their application scope.^[32] A larger driving pressure can yield higher force output and stiffness, improving the efficacy of soft pneumatic actuators. By increasing the maximum driving pressure, pneumatic-based soft sensors can increase their tunable sensing range, allowing them to sense a high-force contact.^[11] Additionally, tunable stiffness

proves beneficial in designing medical tissue or organ simulators for effective medical training.^[33]

Future work will encompass the application of this method to soft-robot design and the development of algorithms for functionally graded soft lattices with unevenly distributed sizes and types, based on robot motion. We also plan to conduct further mechanical tests, including impact testing, as we refine the soft robot for specific operational contexts.

5. Experimental Section

Fabrication: The 3D printing of all samples was done using a multi-material Polyjet 3D printer (J735, Stratasys Ltd., USA) with SUP706B as support material for the lattice samples. All samples were printed with a matte surface finish and standard density support. After printing, the Polyjet's gel-like support materials were later dissolved with chemical bathing in a tank (GEMINI SSR-550) filled with chemical support removal solution (0.02 kg L^{-1} sodium hydroxide and 0.01 kg L^{-1} sodium metasilicate).

FEM Setup: Ansys (Ansys, Inc., USA) was used for the FEM simulation. The material property of the Agilus30 was modeled with a third-order Ogden model with $\mu_1 = 0.2127 \text{ MPa}$, $\alpha_1 = 1.3212$, $\mu_2 = 0.0375 \text{ MPa}$, $\alpha_2 = 4.318$, $\mu_3 = -0.001 \text{ MPa}$, $\alpha_3 = -1.0248$. The material parameters were obtained from literature.^[34] The Poisson's ratio of the material was set as 0.49. The density of the material was set as 1.14 g cm^{-3} . The bottom of the structure was fixed, while a distributed load was applied on the top surface of the structure. The stress and strain information and the top structure surface displacement were recorded. In the FEM study, four types of soft lattices "X", "Grid", "Vintiles", and "Cross" were studied. All samples were designed with strut diameter $d = 1.0 \text{ mm}$.

Characterization Setup: The cartesian robot used for testing the lattice samples was a 3-axis Shibaura BA-III cartesian robot (Toshiba Machine Co., Ltd., Japan). The force exerted by the indenter was measured by a single-point load cell (Model 1006, Tedea-Huntleigh). The internal pressure inside the 3D-printed hemispherical shell with soft lattice reinforcement was controlled by a pressure regulator (VPPE-3-1-1/8-2-010-E1, Festo, Germany).

Acknowledgements

This work was supported by the Engineering and Physical Sciences Research Council (EPSRC) Grant EP/V000748/1; S.W. was supported by the CSC-PAG Oxford Scholarship for his study.

Conflict of Interest

The authors declare no conflict of interest.

Data Availability Statement

The data that support the findings of this study are available from the corresponding author upon reasonable request.

Keywords

3D printing, anti-ballooning, internal constraint, lattice, soft actuator

Received: May 16, 2023
Published online: June 16, 2023

- [1] T. Ranzani, M. Cianchetti, G. Gerboni, I. D. Falco, A. Menciassi, *IEEE Trans. Rob.* **2016**, 32, 187.
- [2] J. Kim, A. Alspach, K. Yamane, in *2015 IEEE/RSJ Int. Conf. on Intelligent Robots and Systems (IROS)*, IEEE, Piscataway, NJ **2015**, pp. 2419–2425.
- [3] L. He, Q. Lu, S. Abad, N. Rojas, T. Nanayakkara, *IEEE Rob. Autom. Lett.* **2020**, 5, 2714.

- [4] L. He, X. Tan, K. Suzumori, T. Nanayakkara, *Sens. Actuators A: Phys.* **2021**, 324, 112674.
- [5] J. Z. Gul, M. Sajid, M. M. Rehman, G. U. Siddiqui, I. Shah, K. H. Kim, J. W. Lee, K. H. Choi, *Sci. Technol. Adv. Mater.* **2018**, 19, 243.
- [6] E. Sacyani Keneth, A. Kamyshny, M. Totaro, L. Beccai, S. Magdassi, *Adv. Mater.* **2020**, 33, 2003387.
- [7] H. K. Yap, H. Y. Ng, C. H. Yeow, *Soft Rob.* **2016**, 3, 144.
- [8] B. N. Peele, T. J. Wallin, H. Zhao, R. F. Shepherd, *Bioinspiration Biomimetics* **2015**, 10, 055003.
- [9] B. Sparrman, C. du Pasquier, C. Thomsen, S. Darbari, R. Rustom, J. Laucks, K. Shea, S. Tibbits, *Addit. Manuf.* **2021**, 40, 101860.
- [10] F. Connolly, C. J. Walsh, K. Bertoldi, *Proc. Natl. Acad. Sci.* **2017**, 114, 51.
- [11] L. He, N. Herzig, T. Nanayakkara, P. Maiolino, *Soft Rob.* **2022**, 9, 1062.
- [12] O. Shorthose, A. Albin, L. He, P. Maiolino, *IEEE Rob. Autom. Lett.* **2022**, 7, 3945.
- [13] A. Zolfagharian, M. A. P. Mahmud, S. Gharai, M. Bodaghi, A. Z. Kouzani, A. Kaynak, *Virtual Phys. Prototyping* **2020**, 15, 373.
- [14] O. Weeger, N. Boddeti, S.-K. Yeung, S. Kaijima, M. L. Dunn, *Addit. Manuf.* **2019**, 25, 39.
- [15] F. Albertini, J. Dirrenberger, C. Sollogoub, T. Maconachie, M. Leary, A. Molotnikov, *Addit. Manuf.* **2021**, 47, 102351.
- [16] J.-H. Park, K. Park, *Addit. Manuf.* **2020**, 33, 101148.
- [17] H. Cho, J. C. Weaver, E. Pösel, P. J. in't Veld, M. C. Boyce, G. C. Rutledge, *Adv. Funct. Mater.* **2016**, 26, 6938.
- [18] S. Y. Choy, C.-N. Sun, K. F. Leong, J. Wei, *Mater. Des.* **2017**, 131, 112.
- [19] L. E. Murr, S. M. Gaytan, D. A. Ramirez, E. Martinez, J. Hernandez, K. N. Amato, P. W. Shindo, F. R. Medina, R. B. Wicker, *J. Mater. Sci. Technol.* **2012**, 28, 1.
- [20] M. Rashed, M. Ashraf, R. Mines, P. J. Hazell, *Mater. Des.* **2016**, 95, 518.
- [21] L. Yang, S. Wu, C. Yan, P. Chen, L. Zhang, C. Han, C. Cai, S. Wen, Y. Zhou, Y. Shi, *Addit. Manuf.* **2021**, 46, 102214.
- [22] R. Xiao, M. Ding, Y. Wang, L. Gao, R. Fan, Y. Lu, *Nanotechnology* **2021**, 32, 35702.
- [23] Z. Sun, Y. Guo, V. Shim, *Int. J. Impact Eng.* **2022**, 160, 104059.
- [24] R. Sala, S. Regondi, S. Graziosi, R. Pugliese, *Addit. Manuf.* **2022**, 58, 102976.
- [25] X. Yu, J. Zhou, H. Liang, Z. Jiang, L. Wu, *Prog. Mater. Sci.* **2018**, 94, 114.
- [26] Y. Jiang, Q. Wang, *Sci. Rep.* **2016**, 6, 34147.
- [27] Y. Yao, L. He, P. Maiolino, in *2022 IEEE 5th Int. Conf. on Soft Robotics (RoboSoft)*, IEEE, Piscataway, NJ **2022**, pp. 29–34.
- [28] W. Ouyang, L. He, A. Albin, P. Maiolino, in *2022 IEEE 5th Int. Conf. on Soft Robotics (RoboSoft)*, IEEE, Piscataway, NJ **2022**, pp. 919–924.
- [29] I. Echeta, B. Dutton, R. K. Leach, S. Piano, *Addit. Manuf.* **2021**, 47, 102301.
- [30] L. He, P. Maiolino, F. Leong, T. Lalitharatne, S. De Lusignan, G. Mazdak, F. Iida, T. Nanayakkara, *IEEE Rev. Biomed. Eng.* **2022**, 16, 514.
- [31] L. He, N. Herzig, S. de Lusignan, T. Nanayakkara, in *2018 40th Annual International Conference of the IEEE Engineering in Medicine and Biology Society (EMBC)*, IEEE, Piscataway, NJ **2018**, pp. 2154–2157.
- [32] M. Manti, V. Cacucciolo, M. Cianchetti, *IEEE Rob. Autom. Mag.* **2016**, 23, 93.
- [33] L. He, N. Herzig, S. de Lusignan, L. Scimeca, P. Maiolino, F. Iida, T. Nanayakkara, *IEEE Trans. Rob.* **2020**, 37, 1051.
- [34] F. F. Abayazid, M. Ghajari, *Addit. Manuf.* **2020**, 33, 101160.